Inorganic Chemistry

Article

pubs.acs.org/IC

Effect of the Axial Ligand on the Reactivity of the Oxoiron(IV) Porphyrin π-Cation Radical Complex: Higher Stabilization of the Product State Relative to the Reactant State

Akihiro Takahashi,[†,‡] Daisuke Yamaki,[∥] Kenichiro Ikemura,[§] Takuya Kurahashi,[†,‡] Takashi Ogura,[§] Masahiko Hada,[∥] and Hiroshi Fujii*[,†,‡]

[†]Institute for Molecular Science and Okazaki Institute for Integrative Bioscience, National Institutes of Natural Sciences, Myodaiji, Okazaki 444-8787, Japan

[‡]Department of Functional Molecular Science, The Graduate University for Advanced Studies (SOKENDAI), Myodaiji, Okazaki 444-8787, Japan

[∥]Department of Chemistry, Graduate School of Science and Engineering, Tokyo Metropolitan University, 1-1 Minami-Osawa, Hachioji, Tokyo 192-0397, Japan

[§]Department of Life Science and Picobiology Institute, Graduate School of Life Science, University of Hyogo, Koto, Kamigori, Ako, Hyogo 678-1297, Japan

Supporting Information

ABSTRACT: The proximal heme axial ligand plays an important role in tuning the reactivity of oxoiron(IV) porphyrin π-cation radical species (compound I) in enzymatic and catalytic oxygenation reactions. To reveal the essence of the axial ligand effect on the reactivity, we investigated it from a thermodynamic viewpoint. Compound I model complexes, $(TMP^{+\bullet})Fe^{IV}O(L)$ (where TMP is 5,10,15,20-tetramesitylporphyrin and $TMP^{+\bullet}$ is its π-cation radical), can be provided with altered reactivity by changing the identity of the axial ligand, but the reactivity is not correlated with spectroscopic data (ν(Fe═O), redox potential, and so on) of $(TMP^{+\bullet})Fe^{IV}O(L)$. Surprisingly, a clear correlation was found between the reactivity of $(TMP^{+\bullet})Fe^{IV}O(L)$ and the Fe^{II}/Fe^{III} redox potential of $(TMP)Fe^{III}L$, the final reaction product. This suggests that the thermodynamic stability of $(TMP)Fe^{III}L$ is involved in the mechanism of the axial ligand effect. Axial ligand-exchange experiments and theoretical calculations demonstrate a linear free-energy relationship, in which the axial ligand modulates the reaction free energy by changing the thermodynamic stability of $(TMP)Fe^{III}(L)$ to a greater extent than $(TMP^{+\bullet})Fe^{IV}O(L)$. The linear free energy relationship could be found for a wide range of anionic axial ligands and for various types of reactions, such as epoxidation, demethylation, and hydrogen abstraction reactions. The essence of the axial ligand effect is neither the electron donor ability of the axial ligand nor the electron affinity of compound I, but the binding ability of the axial ligand (the stabilization by the axial ligand). An axial ligand that binds more strongly makes $(TMP)Fe^{III}(L)$ more stable and $(TMP^{+\bullet})Fe^{IV}O(L)$ more reactive. All results indicate that the axial ligand controls the reactivity of compound I (the stability of the transition state) by the stability of the ground state of the final reaction product and not by compound I itself.

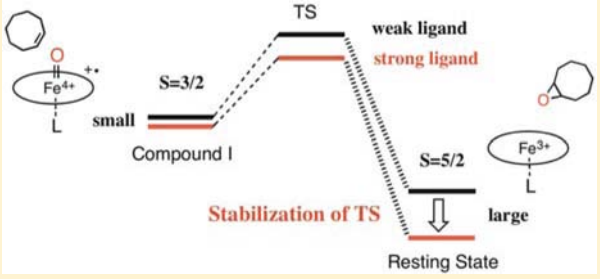

INTRODUCTION

High-valent iron oxo species have been identified as the key reaction intermediates in the catalytic cycles of oxygen activating iron enzymes, as well as synthetic oxygenation catalysts.[1−5] In heme enzymes, an oxoiron(IV) porphyrin π-cation radical species known as compound I has been characterized in the catalytic cycles of peroxidases, catalases, and cytochrome P450s.[6−10] These heme enzymes have the same heme (iron protoporphyrin IX), but different heme proximal (axial) ligands (histidine in peroxidases, tyrosine in catalases, and cysteine in cytochrome P450s). The axial ligands are highly conserved in these heme enzymes.[1,6,11] Therefore, it has been believed that the axial ligand tunes the reactivity of compound I. In particular, it has been suggested that the proximal cysteinate (thiolate) ligand of cytochrome P450 increases the oxidizing power of compound I for hydroxylation of unactivated C−H bonds.[12]

To reveal the functional role of the axial ligand, its effect on the reactivity of high-valent iron oxo species has been studied systematically in synthetic enzyme model complexes. Previously, a pronounced axial ligand effect on the reaction rate of styrene epoxidation was found by investigating synthetic compound I model complexes with various axial anion ligands,

Received: March 30, 2012
Published: June 20, 2012

   dx.doi.org/10.1021/ic3006597 | Inorg. Chem. 2012, 51, 7296−7305

such as chloride, fluoride, and acetate, among others.[13] Recently, the axial ligand effect was studied in detail using other synthetic compound I model systems, and by performing density functional theory (DFT) calculations.[14−19] These studies confirmed that the axial ligand affects the reactivity of compound I. The axial ligand effect on the reactivity was examined to explain it by its electron donor effect and/or the electron affinity of compound I. As the axial ligand becomes a better electron donor, it strengthens the FeO-H bond, increasing hydrogen abstraction activity, and it weakens the Fe═O bond, enhancing oxo-transfer reaction. Although the electron donor effect can explain a narrow range of the axial ligand effect such as *p*-substituent effect of axial ligand,[15c] it cannot be applicable to a wide range of the axial ligand effect. In fact, the electron donor effect of the axial ligand obviously contradicts the previous experimental result.[13] The Fe═O bond strength, ν(Fe═O), of compound I model complex did not correlate with the reaction rate constant.[13] Moreover, reactivity of compound I model complexes having imidazole and phenolate axial ligands did not correlate with their electron donor effects.[20] In addition, a recent report on the redox potential of oxoiron(IV) porphyrin complexes showed that the axial ligand does not change the redox potential (electron affinity) of compound I.[21] These results clearly indicate that there is a more essential factor than these factors.

To reveal the essence of the axial ligand effect on the reactivity of compound I, we have investigated the axial ligand effect with compound I model complexes, $(TMP^{+\bullet})Fe^{IV}O(L)$, where $TMP^{+\bullet}$ is the π-cation radical of 5,10,15,20-tetramesitylporphyrinate (TMP) and L is selected from the following anionic axial ligands: nitrate (NO_3), trifluoroacetate (TFA), acetate (Ac), chloride (Cl), fluoride (F), benzoate (Bz), and hydrocinnamate (Hc) (Figure 1). In this study, we identified a

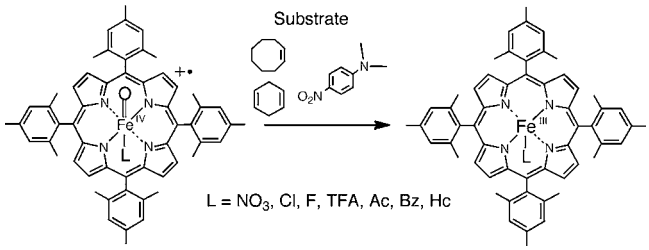

Figure 1. Structures of $(TMP^{+\bullet})Fe^{IV}O(L)$ and $(TMP)Fe^{III}(L)$.

significant correlation between the reaction rate constants of $(TMP^{+\bullet})Fe^{IV}O(L)$ and the redox potential of Fe^{II}/Fe^{III} redox process of $(TMP)Fe^{III}(L)$: the final heme species after the reaction. On the other hand, we could not find a correlation between the reaction rate constant and spectroscopic data of $(TMP^{+\bullet})Fe^{IV}O(L)$. The observed correlation suggests a unique idea that the axial ligand controls the reactivity of compound I by modulating thermodynamic stability of the iron(III) porphyrin species, not by that of compound I itself. This idea was confirmed by the axial ligand exchange experiments for $(TMP^{+\bullet})Fe^{IV}O(L)$ and $(TMP)Fe^{III}(L)$. On the basis of the present results including the DFT calculations, we discuss the essence of the axial ligand effect on the reactivity of compound I.

RESULTS

Electronic Structure and Reactivity. The reactivity of $(TMP^{+\bullet})Fe^{IV}O(L)$, where L is selected from F, Cl, Bz, Ac, Hc, TFA, and NO_3, was evaluated in the reactions with cyclooctene (epoxidation), 1,4-cyclohexadiene (hydrogen abstraction), and *N*,*N*-dimethyl-*p*-nitroaniline (demethylation) (Figure 1). The final species of $(TMP^{+\bullet})Fe^{IV}O(L)$ after reactions with these substrates were the corresponding iron(III) porphyrin complexes, $(TMP)Fe^{III}(L)$. The reactivity data for these reactions are summarized in Supporting Information, Figure S1 and Table 1. All of these reactivity data clearly show a pronounced axial ligand effect, and the reactivity of $(TMP^{+\bullet})Fe^{IV}O(L)$ increases according to the order of L = NO_3 < TFA < Ac < Cl < Hc < Bz < F for each of the three substrates. Summaries of the spectroscopic and electrochemical characterization of $(TMP^{+\bullet})Fe^{IV}O(L)$ and $(TMP)Fe^{III}(L)$ are provided in Supporting Information, Figures S2−S8 and in Table 1. All data for $(TMP^{+\bullet})Fe^{IV}O(L)$ and $(TMP)Fe^{III}(L)$ are consistent with oxoiron(IV) porphyrin π-cation radical complexes in the quartet ground state (S = 3/2: ferromagnetic coupling of iron(IV) S = 1 and porphyrin π-cation radical S = 1/2) and iron(III) porphyrin complexes in the sextet ground state (S =5/2: iron(III) high-spin), respectively.[22,23]

To explore the potential factors controlling the reactivity of $(TMP^{+\bullet})Fe^{IV}O(L)$, we examined the correlation between the reaction rate constants and the spectroscopic parameters shown in Table 1. If the axial ligand activates compound I model complex, the reaction rate constants of $(TMP^{+\bullet})Fe^{IV}O(L)$ are expected to be correlated with particular spectroscopic parameters of $(TMP^{+\bullet})Fe^{IV}O(L)$, such as Fe═O bond strength: ν(Fe═O), redox potential, ^{1}H NMR shift, and EPR *g*-parameters of $(TMP^{+\bullet})Fe^{IV}O(L)$.[15−17] However, we could not identify any significant correlations with these spectroscopic parameters. Although previous studies proposed the electron donor ability of the axial ligand and electron affinity of $(TMP^{+\bullet})Fe^{IV}O(L)$ as a key of the axial ligand effect, this study reveals that these factors are not the essence of the axial ligand effect. Interestingly, as shown in Figure 2, we identified a significant correlation between the reaction rate constants of $(TMP^{+\bullet})Fe^{IV}O(L)$ and the redox potential of Fe^{II}/Fe^{III} redox process of $(TMP)Fe^{III}(L)$: the final porphyrin species after the reaction. Other spectroscopic parameters of $(TMP)Fe^{III}(L)$ in Table 1 were not correlated with the reactivity data of $(TMP^{+\bullet})Fe^{IV}O(L)$.

The $E_{1/2}$ values for the Fe^{II}/Fe^{III} redox couple of $(TMP)Fe^{III}(L)$, which is governed by the Nernst equation, depends on the relative interactions of both $[(TMP)Fe^{III}]^+$ and $(TMP)Fe^{II}$ with the axial ligand (L).[24] The binding constant of the anionic axial ligand (L) to the ferric porphyrin complex is much larger than that to the ferrous porphyrin complex because of the overall positive charge of the ferric porphyrin complex (the porphyrin itself has a −2 charge while ferric iron has a +3 charge). In fact, the binding constant of fluoride, which binds strongly to the ferrous porphyrin complex, was estimated to be only ~600.[24] Therefore, the $E_{1/2}$ value for the Fe^{II}/Fe^{III} redox couple of $(TMP)Fe^{III}(L)$ is mainly controlled by the binding constant of $(TMP)Fe^{III}(L)$. The binding constant indicates the thermodynamic stability of $(TMP)Fe^{III}(L)$ relative to $[(TMP)Fe^{III}]^+$. Thus, the correlations observed in Figure 2 suggest that the reactivity of $(TMP^{+\bullet})Fe^{IV}O(L)$ is correlated with the thermodynamic stability of $(TMP)Fe^{III}(L)$.

Axial Ligand Effect on the Free Energy of Reaction. To investigate the axial ligand effect on thermodynamic stability, we estimated the thermodynamic stabilities of $(TMP^{+\bullet})Fe^{IV}O(L)$ and $(TMP)Fe^{III}(L)$ in ligand exchange reactions. Figure 3 shows the ^{1}H NMR spectral change which occurs during a

dx.doi.org/10.1021/ic3006597 | Inorg. Chem. 2012, 51, 7296−7305

Table 1. Spectroscopic and Reactivity Data for $(TMP^{+\bullet})Fe^{IV}O(L)$ and $(TMP)Fe^{III}(L)$ in Dichloromethane at 213 K

L		NO_3	TFA	Ac	Cl	Hc	Bz	F
				$(TMP^{+\bullet})Fe^{IV}O(L)$				
absorption/nm		403, 666	406, 666	409, 668	411, 668	413, 668	410, 670	409, 666
Raman: $\nu_{Fe=O}/cm^{-1}$		821	816	800	804 (801)[a]	802	804	801[a] (807)[b]
EPR: g-value (E/D)		4.44 3.52, 1.98 (0.075)	4.45, 3.52, 1.98 (0.075)	4.45, 3.51, 1.97 (0.075)	4.25, 3.75, 1.99 (0.040)	4.46, 3.50, 1.97 (0.075)	4.45, 3.55, 1.98 (0.075)	4.44 3.52, 1.98 (0.075)
^{1}H NMR	: py-H	−17.3	−13.5	−7.5	−5.8	−7.6	−8.7	−11.5
/ppm from TMS	: *m*-H	64.0, 64.4	58.7, 59.7	65.7	54.8	61.9, 62.7	59.4, 61.0	63.4, 63.9
redox potential/V vs SCE[c]		0.95	0.96	1.04	0.97	nd	0.99	0.96
				$(TMP)Fe^{III}(L)$				
absorption/nm		411, 512, 578, 693	413, 509, 579, 693	414, 502, 567, 675	418, 509, 576, 696	415, 503, 566, 676	414, 503, 569, 678	414, 484, 548, 615
EPR: g-value		6.2, 5.7, 2.0 7.9, 3.8, 1.8	6.0, 2.0	6.0, 2.0	6.0, 2.0	6.0, 2.0	6.0, 2.0 6.1, 5.9, 2.0	6.0, 2.0
^{1}H NMR	: py-H	104.7	105.3	110.0	113.0	110.3	110.1	112.3
/ppm from TMS	: *m*-H	21.5, 19.4	19.3, 17.1	17.4, 15.5	20.5, 18.0	17.5, 15.5	17.6, 15.6	15.7, 14.0
redox potential/V vs SCE		−0.18	−0.32	−0.46	−0.45	−0.48	−0.51	−0.63
				Second-Order Reaction Rate Constant at 213 K (k_2: M^{-1} s^{-1})				
cyclooctene ($\times 10^{-2}$)		1.5 ± 0.1	4.7 ± 0.1	5.0 ± 0.1	9.1 ± 0.2	14.9 ± 0.1	20.1 ± 0.3	29.4 ± 4.4
N,N-dimethyl-*p*-nitroaniline		1.6 ± 0.1	3.2 ± 0.1	6.3 ± 0.1	6.4 ± 0.1	12.6 ± 0.1	14.9 ± 0.2	29.7 ± 2.0
1,4-cyclohexadiene		3.6 ± 0.1	5.9 ± 0.1	11.9 ± 0.1	12.6 ± 0.1	16.4 ± 0.2	19.8 ± 0.1	24.0 ± 0.1
				Thermodynamic Parameters at 213 K (kJ/mol)				
$\Delta(\Delta G_{EX})$		0.0	7.7	11.5	22.6	18.2	20.3	34.1
$\Delta G^{\ddagger}_{Cyclooctene}$		59.0 ± 0.1	57.0 ± 0.1	56.9 ± 0.1	55.8 ± 0.1	54.9 ± 0.1	54.4 ± 0.1	53.7 ± 0.3
$\Delta G^{\ddagger}_{N,N\text{-Dimethyl-}p\text{-nitroaniline}}$		50.7 ± 0.1	49.5 ± 0.1	48.3 ± 0.1	48.3 ± 0.1	47.1 ± 0.1	46.8 ± 0.1	45.6 ± 0.1
$\Delta G^{\ddagger}_{1,4\text{-Cyclohexadiene}}$		49.3 ± 0.1	48.4 ± 0.1	47.2 ± 0.1	47.1 ± 0.1	46.6 ± 0.1	46.3 ± 0.1	45.9 ± 0.1

[a]Ref 37. [b]Ref 38. [c]Ref 21.

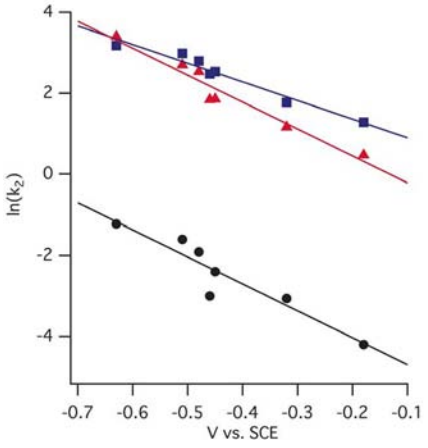

Figure 2. Plot of *ln* of the reaction rate constants (k_2) of the reaction of $(TMP^{+\bullet})Fe^{IV}O(L)$ with cyclooctene (black circle), *N,N*-dimethyl-*p*-nitroaniline (red triangle), and 1,4-cyclohexadiene (blue square) vs the redox potential for Fe^{II}/Fe^{III} redox process of $(TMP)Fe^{III}(L)$.

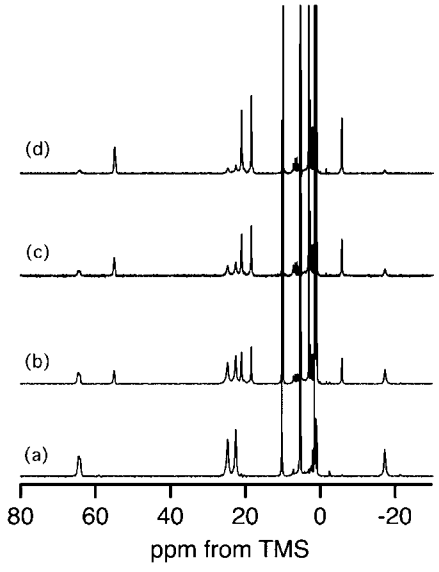

Figure 3. ^{1}H NMR spectral change for the titration of $(TMP^{+\bullet})Fe^{IV}O(NO_3)$ with *n*-$Bu_4N(Cl)$ in CD_2Cl_2 at −60 °C. (a) $(TMP^{+\bullet})Fe^{IV}O(NO_3)$, (b) (a) + 0.5 equiv of *n*-$Bu_4N(Cl)$, (c) (a) + 1.0 equiv of *n*-$Bu_4N(Cl)$, (d) (a) + 1.5 equiv of *n*-$Bu_4N(Cl)$.

titration of $(TMP^{+\bullet})Fe^{IV}O(NO_3)$ with tetra-*n*-butylammonium chloride (*n*-$Bu_4N(Cl)$) at −60 °C. Upon addition of *n*-$Bu_4N(Cl)$, the ^{1}H NMR spectrum of $(TMP^{+\bullet})Fe^{IV}O(NO_3)$ changes to that of $(TMP^{+\bullet})Fe^{IV}O(Cl)$ because of axial ligand exchange according to the following equation:

$$(TMP^{+\bullet})Fe^{IV}O(L_1) + n\text{Bu}_4N(L_2) \rightleftarrows (TMP^{+\bullet})Fe^{IV}O(L_2) + n\text{Bu}_4N(L_1) \quad (1)$$

where L_1 and L_2 are nitrate and chloride, respectively. The ratio of $(TMP^{+\bullet})Fe^{IV}O(NO_3)$ to $(TMP^{+\bullet})Fe^{IV}O(Cl)$ was determined by peak areas of their mesityl meta protons and pyrrole-β protons in the ^{1}H NMR spectra. The equilibrium constant for the ligand exchange reaction was estimated to be $K = 6 \pm 1$ (see Experimental Section). The difference in thermodynamic stability between $(TMP^{+\bullet})Fe^{IV}O(NO_3)$ and $(TMP^{+\bullet})Fe^{IV}O(Cl)$ for eq 1 was estimated to be $(\Delta G_{EX}) = -3.2 \pm 0.3$ kJ/mol at 213 K from the relationship, $\Delta G = -RT\ ln\ K$.[25,26] We performed similar experiments for $(TMP^{+\bullet})Fe^{IV}O(L)$ with the remaining ligands. The results are summarized in Supporting

dx.doi.org/10.1021/ic3006597 | Inorg. Chem. 2012, 51, 7296−7305

Information, Table S1 and thermodynamic stabilities of $(TMP^{+\bullet})Fe^{IV}O(L)$ relative to $(TMP^{+\bullet})Fe^{IV}O(NO_3)$, $(\Delta G_{EX})_{Fe=O}$, are shown in Figure 4.

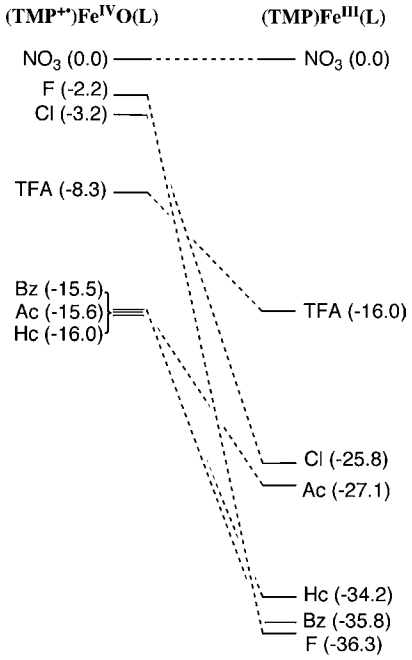

Figure 4. Thermodynamic stabilities (kJ/mol) of $(TMP^{+\bullet})Fe^{IV}O(L)$ (left) and $(TMP)Fe^{III}(L)$ (right) relative to $(TMP^{+\bullet})Fe^{IV}O(NO_3)$ and $(TMP)Fe^{III}(NO_3)$, respectively.

Similarly, ligand exchange reactions for $(TMP)Fe^{III}(L)$ were also examined with various tetra-*n*-butylammonium salts as follows.

$$(TMP)Fe^{III}(L_1) + nBu_4N(L_2) \rightleftarrows (TMP)Fe^{III}(L_2) + nBu_4N(L_1) \quad (2)$$

The results are summarized in Supporting Information, Table S2, and the thermodynamic stability values of $(TMP)Fe^{III}(L)$ relative to $(TMP)Fe^{III}(NO_3)$, $(\Delta G_{EX})_{Fe(III)}$, are also summarized in Figure 4. It is obvious that the axial ligand effect on thermodynamic stability for $(TMP)Fe^{III}(L)$ is more significant than that for $(TMP^{+\bullet})Fe^{IV}O(L)$.

From these results, we estimated the changes in free energy of the transition from $(TMP^{+\bullet})Fe^{IV}O(L)$ to $(TMP)Fe^{III}(L)$ with eq 3 derived from eq 2 − eq 1, where L_2 is nitrate.

$$(TMP^{+\bullet})Fe^{IV}O(NO_3) + (TMP)Fe^{III}(L_1) \rightleftarrows (TMP^{+\bullet})Fe^{IV}O(L_1) + (TMP)Fe^{III}(NO_3) \quad (3)$$

In eq 3, n-$Bu_4N(L_1)$ and n-$Bu_4N(NO_3)$, appearing in eqs 1 and 2, are canceled by the subtraction. Obviously, the ΔG value for eq 3, $\Delta(\Delta G_{EX})$, indicates the difference of the change in free energy between the transitions from $(TMP^{+\bullet})Fe^{IV}O(L_1)$ to $(TMP)Fe^{III}(L_1)$ and from $(TMP^{+\bullet})Fe^{IV}O(NO_3)$ to $(TMP)Fe^{III}(NO_3)$, and can be easily calculated from the difference between the $(\Delta G_{EX})_{Fe=O}$ and $(\Delta G_{EX})_{Fe(III)}$, shown in Figure 4. We calculated $\Delta(\Delta G_{EX})$ values for all axial ligands, and the estimated $\Delta(\Delta G_{EX})$ values are listed in Table 1.

When the logarithm (*ln*) values of the reaction rate constants for the cyclooctene epoxidation of $(TMP^{+\bullet})Fe^{IV}O(L)$ are plotted against their estimated $\Delta(\Delta G_{EX})$ values, a consistent linear behavior is found (Figure 5). Since the logarithm (*ln*) of the reaction rate constant indicates the free energy of activation

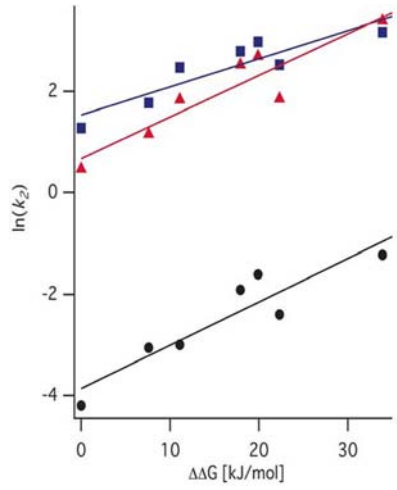

Figure 5. Plot of *ln* of the reaction rate constants (k_2) of $(TMP^{+\bullet})Fe^{IV}O(L)$ with cyclooctene (black circle), *N*,*N*-dimethyl-*p*-nitroaniline (red triangle), and 1,4-cyclohexadiene (blue square) vs the $\Delta\Delta G$ value estimated from ligand exchange.

($\Delta G^{\ddagger}$), the observed linear correlation is consistent with the Brønsted−Evans−Polanyi relationship, eq 4, which directly relates the change in the free energy of activation, $\Delta\Delta G^{\ddagger}$, to the corresponding change of free energy of its reaction, $\Delta\Delta G_r$, via a constant factor α ($0 < \alpha < 1$).[27−30]

$$\Delta\Delta G^{\ddagger} = \beta\Delta\Delta G_r \quad (4)$$

From the slope of the line in Figure 5, we calculated the α to be 0.15 for the cyclooctene epoxidation reaction. An α value close to 0 indicates an early transition state that is structurally similar to the initial reactant state, while an α value close to 1 indicates a late transition state which is structurally similar to the product state. The estimated α value indicates an early transition state for the cyclooctene epoxidation reaction of $(TMP^{+\bullet})Fe^{IV}O(L)$. The α value estimated in this study was very close to that (0.18) for an epoxidation reaction of norbornene with oxochromium(V) porphyrin complex.[31] This suggests that the transition state structure of the epoxidation reaction of $(TMP^{+\bullet})Fe^{IV}O(L)$ is similar to that of oxochromium(V) porphyrin complex, which has been proposed as a charge-transfer complex.[31]

Consistent linear relationships were also found for other oxidation reactions of $(TMP^{+\bullet})Fe^{IV}O(L)$. As shown in Figure 5, the logarithm of the reaction rate constants of the reactions of $(TMP^{+\bullet})Fe^{IV}O(L)$ with 1,4-cyclohexadiene and *N*,*N*-dimethyl-*p*-nitroaniline show a consistent linear relationship with the $\Delta(\Delta G_{EX})$ values. The α values for 1,4-cyclohexadiene and *N*,*N*-dimethyl-*p*-nitroaniline were estimated to be 0.10 and 0.15, respectively. The α value for *N*,*N*-dimethyl-*p*-nitroaniline was the same as that for cyclooctene, but the value for 1,4-cyclohexadiene was found to be smaller.

Quantum Chemical Calculations. To further study the axial ligand effect, we performed DFT calculations for epoxidation reactions of cyclooctene with $(TMP^{+\bullet})Fe^{IV}O(L)$. To simplify the systems for calculations, we replaced the meso-mesityl group of the TMP ligand with a hydrogen atom and performed a calculation for the porphine (Por) complex. The

dx.doi.org/10.1021/ic3006597 | *Inorg. Chem.* 2012, 51, 7296−7305

optimized structures and bond lengths for $(Por^{+\bullet})Fe^{IV}O(L)$ and $(Por)Fe^{III}(L)$, where L = F, Cl, Bz, Ac, TFA, and NO_3, are shown in Supporting Information, Figures S9 and S10 and Table S3. Figure 6 shows the energy profiles of the four lowest-lying spin states of $(Por^{+\bullet})Fe^{IV}O(L)$ and $(Por)Fe^{III}(L)$. The ground states for all of the $(Por^{+\bullet})Fe^{IV}O(L)$ complexes are in the quartet (S = 3/2) state, in which the two electron spins in iron dπ (d_{xz} and d_{yz}) orbitals are ferromagnetically coupled with the porphyrin π-cation radical spin in the a_{2u} orbital. The doublet (S =1/2) states, in which the iron d_π electron spins antiferromagnetically couple with the a_{2u} radical spin, are slightly higher than the ground quartet states. There are two excited states, the sextet (S = 5/2) and the quartet (S = 3/2) states, in which four unpaired electrons in iron d-orbitals (d_{xy}, d_{xz}, d_{yz}, $d_{x^2-y^2}$) interact with an unpaired electron in the a_{2u} orbital. The ground states of $(P)Fe^{III}(L)$ are the sextet (high-spin S = 5/2) states with unpaired electrons in all five d orbitals. There were two excited quartet (intermediate-spin S = 3/2) states with unpaired electrons in the d_{xz}, d_{yz}, d_{z^2} orbitals and d_{xz}, d_{yz}, $d_{x^2-y^2}$ orbitals. The doublet (low-spin S = 1/2) states have the highest energies of all states of $(Por)Fe^{III}(L)$ complexes. The results of the present DFT calculations are consistent with the spectroscopic characterization of $(TMP^{+\bullet})Fe^{IV}O(L)$ and $(TMP)Fe^{III}(L)$ and previous DFT calculations of other compound I model complexes.[15b,d,17c,18c]

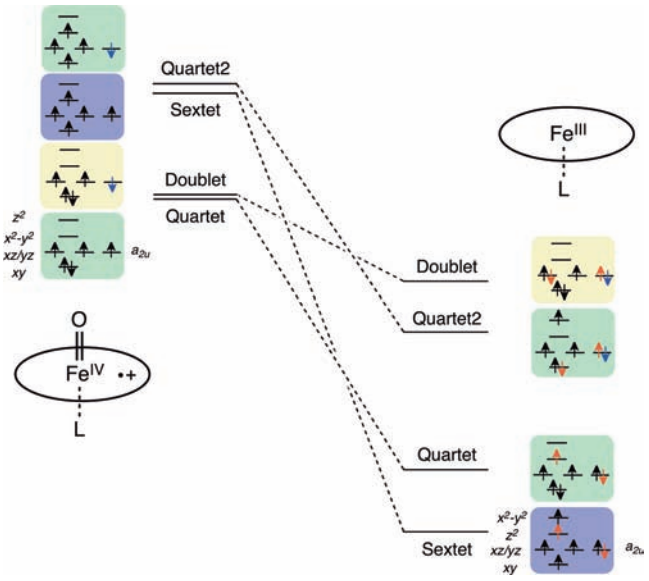

Figure 6. Energy profile for the reaction of $(Por^{+\bullet})Fe^{IV}O(F)$ with cyclooctene. The structure and states on the left side are for $(Por^{+\bullet})Fe^{IV}O(L)$ and cyclooctene, and the structure and states on the right side are for $(Por)Fe^{III}(L)$ and cyclooctene oxide.

Table 2 shows energies of these spin states relative to the ground state of $(Por^{+\bullet})Fe^{IV}O(L)$ before and after cyclooctene epoxidation. The energies of these spin states of $(Por^{+\bullet})Fe^{IV}O(L)$ and $(Por)Fe^{III}(L)$ were changed by the axial ligand effect. The axial ligand effect on the energies of the spin states for $(Por)Fe^{III}(L)$ were found to be more pronounced than those for $(Por^{+\bullet})Fe^{IV}O(L)$. This is consistent with the ligand exchange experiments. The energies of the sextet ground state of $(Por)Fe^{III}(L)$ in Table 2 indicate an enthalpy change (ΔH_{DFT}) during the cyclooctene epoxidation reaction promoted by $(Por^{+\bullet})Fe^{IV}O(L)$. The negative ΔH_{DFT} values indicate exothermic reactions. The ΔH_{DFT} values are changed by the axial ligands and increase according to the order of L = TFA < NO_3 < Bz < Ac < Cl < F. This order is not identical to the order of reaction rate constants and $\Delta(\Delta G_{EX})$, but is generally similar.

To compare the axial ligand effect on $(Por^{+\bullet})Fe^{IV}O(L)$ and $(Por)Fe^{III}(L)$, we calculated the binding energies (ΔE_{bound}) of the axial ligands (Table 2). The estimated ΔE_{bound} values from the calculations are fairly large because of the absence of solvation effects with respect to the free axial anion ligand (the calculations were made in the gas phase). For both $(Por^{+\bullet})Fe^{IV}O(L)$ and $(Por)Fe^{III}(L)$, the ΔE_{bound} value increases according to the order of L = NO_3 < TFA < Cl < Bz < Ac < F. The ΔE_{bound} values for $(Por)Fe^{III}(L)$ are larger than those for $(Por^{+\bullet})Fe^{IV}O(L)$ and the axial ligand effect on the ΔE_{bound} value for $(Por)Fe^{III}(L)$ is more significant than that for $(Por^{+\bullet})Fe^{IV}O(L)$.

DISCUSSION

Linear Free Energy Relationship for the Axial Ligand Effect. The observed linear correlation between *ln* of the reaction rate constants of $(TMP^{+\bullet})Fe^{IV}O(L)$ and the change of free energy from $(TMP^{+\bullet})Fe^{IV}O(L)$ to $(TMP)Fe^{III}(L)$ for various anionic axial ligands indicate that the axial ligand controls the reactivity of $(TMP^{+\bullet})Fe^{IV}O(L)$ by modulating the free energy of the overall reaction. This linear free energy relationship can be understood by examining the two-dimensional representation of the crossing potential energy surfaces: curve crossing diagram (Figure 7).[30,32] Curve V_1 represents the potential energy of the one-dimensional system before the reaction (the reactant state), and curve V_2 follows that of the product state. The crossing point of the two potential curves is regarded as the transition state, and the energy from the local minimum of the reactant state (curve V_1)

Table 2. Energies (kJ/mol) of the Four Lowest-Lying Spin States of $(Por^{+\bullet})Fe^{IV}O(L)$ and $(Por)Fe^{III}(L)$ Relative to the Ground States of $(Por^{+\bullet})Fe^{IV}O(L)$

	$(Por^{+\bullet})Fe^{IV}O(L)$					$(Por)Fe^{III}(L)$				
L	doublet	quartet	quartet2	sextet	E_{bound}	doublet	quartet	quartet2	sextet[a]	E_{bound}[b]
NO_3	0.6	0.0	67.1	62.6	447.6	−107.5	−163.9	−110.0	−184.1 (0)	489.5 (−41.9/0)
TFA	0.7	0.0	66.4	61.7	457.2	−98.7	−163.2	−105.7	−182.8 (−1.2)	497.9 (−40.7/ −1.2)
Cl	0.6	0.0	64.7	61.4	466.4	−91.6	−172.8	−119.9	−200.4 (16.3)	524.7 (−58.3/16.3)
Ac	1.3	0.0	66.7	62.2	517.6	−107.9	−169.5	−116.2	−198.1 (14.0)	573.5 (−55.9/14.0)
Bz	0.9	0.0	65.6	61.2	478.1	−106.6	−169.5	−115.1	−196.9 (12.8)	532.8 (−54.7/12.8)
F	0.9	0.0	57.0	52.3	799.2	−97.2	−186.6	−125.8	−218.4 (34.3)	875.4 (−76.2/34.3)

[a]The numbers in parentheses are the difference between $(Por)Fe^{III}(NO_3)$ and $(Por)Fe^{III}(L)$. [b]The numbers in parentheses are the difference of binding energies from $(Por^{+\bullet})Fe^{IV}O(L)$ to $(Por)Fe^{III}(L)$ and the change in the difference from the nitrate complex.

dx.doi.org/10.1021/ic3006597 | Inorg. Chem. 2012, 51, 7296−7305

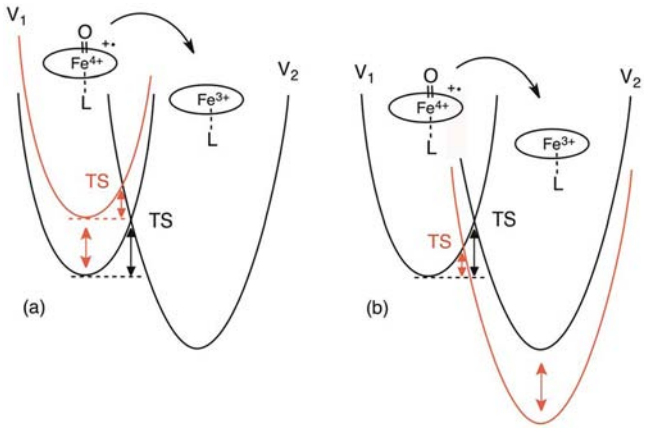

Figure 7. Curve crossing diagram of potential-energy surfaces of the reactant, $(TMP^{+\bullet})Fe^{IV}O(L)$, and product, $(TMP)Fe^{III}(L)$, states. V_1 and V_2 indicate the potential curves of $(TMP^{+\bullet})Fe^{IV}O(L)$ and $(TMP)Fe^{III}(L)$, respectively. TS is the transition state of the reaction. (a) Change of stability of $(TMP^{+\bullet})Fe^{IV}O(L)$ and (b) change of stability of $(TMP)Fe^{III}(L)$.

to the crossing point represents the activation energy of the reaction. The diagram shown in Figure 7 is too simple to describe a reaction pathway of $(TMP^{+\bullet})Fe^{IV}O(L)$ with a substrate because many previous studies have proposed stepwise mechanisms via radical intermediates.[18,21,32−34] We use this simplified diagram to easily understand the observed linear free energy relationship, and then expand the diagram into the stepwise mechanism. When the reactant state is destabilized or the product state is stabilized by the axial ligand effect, the ΔG_r value becomes larger, the transition state moves to the reactant state, and the activation energy becomes smaller. In contrast, when the reactant state is stabilized or the product state is destabilized by the axial ligand, the ΔG_r becomes smaller, the transition state moves to the product state, and the activation energy becomes larger. As a result, the activation energy (*ln* of reaction rate constants) shows a linear correlation with the free energy of the overall reaction.

Obviously, the activation energy and reaction free energy are altered by the stabilities of the reactant and product states. The answer to the following question should be determined: which state controls these energies? As shown in Figure 4, the axial ligand affects the stability of both $(TMP^{+\bullet})Fe^{IV}O(L)$ and $(TMP)Fe^{III}(L)$; however, the axial ligand effect alters the stability of $(TMP)Fe^{III}(L)$ much more significantly than the stability of $(TMP^{+\bullet})Fe^{IV}O(L)$. This is further confirmed by the present DFT calculations (Table 2). The activation energy of the reaction (the reactivity of $(TMP^{+\bullet})Fe^{IV}O(L)$) is governed by the stability of the product state, $(TMP)Fe^{III}(L)$, more than that of reactant state, $(TMP^{+\bullet})Fe^{IV}O(L)$.

The mechanism we have identified where reactivity of $(TMP^{+\bullet})Fe^{IV}O(L)$ is controlled by the thermodynamic stability of $(TMP)Fe^{III}(L)$ is very unique. An essential point to consider is why the axial ligand changes the stability of $(TMP)Fe^{III}(L)$ much more than that of $(TMP^{+\bullet})Fe^{IV}O(L)$. This can be explained by the trans-ligand effect of the axial ligand. $(TMP^{+\bullet})Fe^{IV}O(L)$ is a six-coordinate complex, but $(TMP)Fe^{III}(L)$ is a five-coordinate complex. The binding of the axial ligand (L) to $[(TMP^{+\bullet})Fe^{IV}O]^+$ becomes weaker than the binding of (L) to $[(TMP)Fe^{III}]^+$ because of the trans-ligand effect provided by the strong oxo ligand. Moreover, the porphyrin π-cation radical character of compound I also may be related to this mechanism. The positive charge of $[(TMP^{+\bullet})Fe^{IV}O]^+$ is delocalized over the heme plane because of the porphyrin π-cation radical character. In contrast, the positive charge of $[(TMP)Fe^{III}]^+$ resides mainly on the heme iron center. Therefore, the binding interaction of an anionic axial ligand with $[(TMP)Fe^{III}]^+$ is stronger than the corresponding binding to $[(TMP^{+\bullet})Fe^{IV}O]^+$. These factors lead to stabilization of $[(TMP)Fe^{III}]^+$ by the anionic axial ligand more than $[(TMP^{+\bullet})Fe^{IV}O]^+$. More generally, as the reaction stage shifts from $(TMP^{+\bullet})Fe^{IV}O(L)$ to $(TMP)Fe^{III}(L)$, the binding of the axial ligand becomes stronger and the stabilization by the axial ligand becomes larger because the iron−oxygen bond length becomes longer (Figure 8). As a result, the transition state is

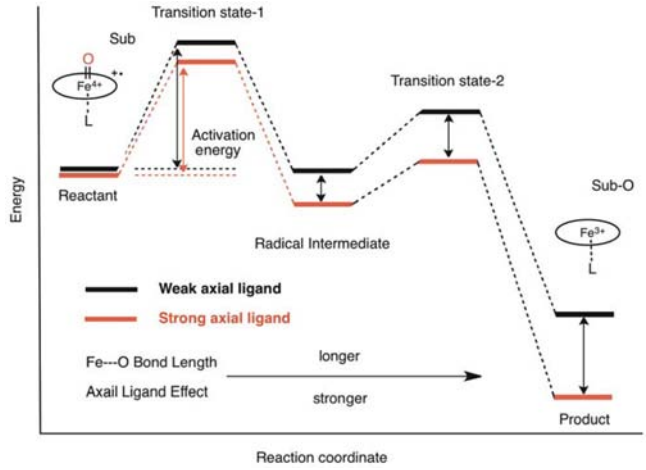

Figure 8. Cartoon of the axial ligand effect on energy profiles along the reaction of $(TMP^{+\bullet})Fe^{IV}O(L)$ with a substrate in a stepwise mechanism. The black lines are the cases for the weak binding axial ligand and the red line is that for strong ones.

stabilized more than $(TMP^{+\bullet})Fe^{IV}O(L)$ by the axial ligand, and the activation energy becomes smaller as the binding of the axial ligand becomes stronger. This is a key point of the axial ligand effect. Previously, the axial ligand effect had been believed to represent the electron-donor effect to compound I and an intermediate and the electron affinity of compound I.[15−18] However, as shown here, the essence of the axial ligand effect is provided by the extent of the stabilization of the product state by the binding of the axial ligand. An axial ligand that binds stronger makes compound I more reactive.

The diagram shown in Figure 7 represents the reaction surface for the direct (concerted) oxygen transfer to a substrate. Since the previous studies proposed that reactions of $(TMP^{+\bullet})Fe^{IV}O(L)$ with substrates proceed stepwise via radical intermediates,[18,21,32,34] we discuss the axial ligand effect on the reactivity for the stepwise mechanism. In the stepwise mechanism, a radical intermediate is more stable than the transition state for the direct oxygen transfer and the potential curve for the radical intermediate cuts through the higher-energy ridge for the direct oxygen transfer and splits the process into two steps (Figure 9). Obviously, the transition state of the first step (TS1) is controlled by the stabilities of $(TMP^{+\bullet})Fe^{IV}O(L)$ and the radical intermediate, but it does not directly connect with $(TMP)Fe^{III}(L)$, and the transition state of the second step (TS2) is controlled by the stabilities of the radical intermediate and $(TMP)Fe^{III}(L)$. As discussed above, the axial ligand effect becomes stronger in the order of

dx.doi.org/10.1021/ic3006597 | *Inorg. Chem.* 2012, 51, 7296−7305

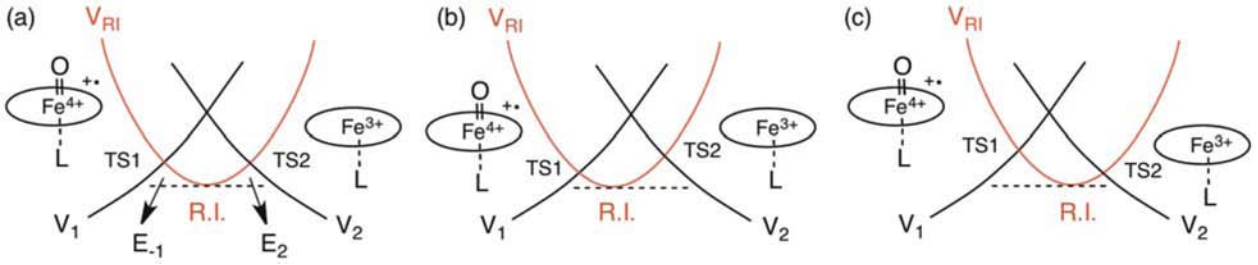

Figure 9. Curve crossing diagram of potential-energy surfaces from $(TMP^{+\bullet})Fe^{IV}O(L)$ to $(TMP)Fe^{III}(L)$ for a stepwise mechanism. V_1 and V_2 indicate the potential curves of $(TMP^{+\bullet})Fe^{IV}O(L)$ and $(TMP)Fe^{III}(L)$, respectively. V_{RI} shows the potential curve of a radical intermediate (R.I.). E_{-1} is the activation energy from R.I. to $(TMP^{+\bullet})Fe^{IV}O(L)$ and E_2 is the activation energy from R.I. to $(TMP)Fe^{III}(L)$. (a) $E_1 \approx E_2$, (b) $E_1 \ll E_2$, and (c) $E_1 \gg E_2$.

$(TMP^{+\bullet})Fe^{IV}O(L)$ < TS1 < the radical intermediate < TS2 < $(TMP)Fe^{III}(L)$ because the iron−oxygen bond length increases in this order (Figure 8).

There are three possible situations in the stepwise mechanism (Figure 9). When the activation energy (E_{-1}) from the radical intermediate to $(TMP^{+\bullet})Fe^{IV}O(L)$ is close to that (E_2) from the radical intermediate to $(TMP)Fe^{III}(L)$ (Figure 9a), the stability of $(TMP)Fe^{III}(L)$ controls the reactivity of $(TMP^{+\bullet})Fe^{IV}O(L)$ because it changes the activation energy E_2. This is confirmed by a kinetic analysis for the stepwise mechanism, in which the overall reaction rate (k) can be derived as $k = k_1/(1 + k_{-1}/k_2)$ using the steady-state approximation, where k_1 is the reaction rate from $(TMP^{+\bullet})Fe^{IV}O(L)$ to the radical intermediate, k_{-1} is the reaction rate of the back reaction, and k_2 is the reaction rate from the radical intermediate to $(TMP)Fe^{III}(L)$. When E_{-1} becomes much smaller than E_2 (Figure 9b, $k_{-1} \gg k_2$), the overall reaction rate can be simplified as $k = k_1k_2/k_{-1}$. This is the case where the potential curve of the radical intermediate shifts to that of $(TMP^{+\bullet})Fe^{IV}O(L)$ or $(TMP)Fe^{III}(L)$ is much destabilized more than $(TMP^{+\bullet})Fe^{IV}O(L)$. TS2 is the transition state of the overall reaction. Therefore, the stability of $(TMP)Fe^{III}(L)$ controls the reactivity of $(TMP^{+\bullet})Fe^{IV}O(L)$ even in this situation. On the other hand, when E_{-1} becomes much larger than E_2 (Figure 9c, $k_{-1} \ll k_2$), the overall reaction rate can be simplified as $k = k_1$. This is the case where the potential curve of the radical intermediate shifts to that of $(TMP)Fe^{III}(L)$ or $(TMP)Fe^{III}(L)$ is much more stabilized than $(TMP^{+\bullet})Fe^{IV}O(L)$. TS1 is the transition state of the overall reaction. The stability of $(TMP)Fe^{III}(L)$ does not directly control the reactivity of $(TMP^{+\bullet})Fe^{IV}O(L)$ in this situation. If the reaction occurs in this situation, TS1 must be controlled by the stability of the radical intermediate because a good correlation of the reaction rate with the stability of $(TMP^{+\bullet})Fe^{IV}O(L)$ could not be observed. This is consistent with the axial ligand effect discussed here (Figure 8). Moreover, the observed correlation of the reactivity of $(TMP^{+\bullet})Fe^{IV}O(L)$ with the stability of $(TMP)Fe^{III}(L)$ suggests the strong correlation of the radical intermediate with $(TMP)Fe^{III}(L)$. When the spin state of the radical intermediate is the same as that of $(TMP)Fe^{III}(L)$, the diagram of Figure 9c can be simplified as Figure 7b and the axial ligand effect would be interpreted with the stability of $(TMP)Fe^{III}(L)$.

Previous computational studies linked the axial ligand effect with the bond dissociation energy (BDE_{O-H}) of the O−H bond in (Por)FeOH(L).[18,19] This is also a linear free energy relationship and can be interpreted by Figure 7. While BDE_{O-H} is changed by the stability of $(Por^{+\bullet})Fe^{IV}O(L)$ and/or (Por)FeOH(L), this study suggests that it is controlled by the stability of (Por)FeOH(L). However, the calculated BDE_{O-H} values do not correlate with the experimental results for the reactivity of $(TMP^{+\bullet})Fe^{IV}O(L)$ reported here and in a previous paper.[20] The order (L = Cl < TFA ≈ Ac < F) of the reactivity estimated from calculated BDE_{O-H} values is different from the experimental results (TFA < Ac < Cl < F).[18c] In addition, $(TMP^{+\bullet})Fe^{IV}O(L)$ has been reported to be very reactive when L is imidazole,[20] but it is expected to be very inactive from BDE_{O-H} calculations.[18a,b] Solvent effect may affect the stability of the radical intermediate and $(TMP)Fe^{III}(L)$, leading to the change of the reactivity between in gas phase and in solution.

The linear free energy relationship was observed not only for epoxidation of cyclooctene, but also for demethylation of *N*,*N*-dimethyl-*p*-nitroaniline and hydrogen abstraction from 1,4-cyclohexadiene. Although the reaction mechanism and transition state of these reactions are different from those of the epoxidation reaction, the same mechanism is also applicable to the axial ligand effect on the reactivity for these reactions.

In this study, the linear free energy relationship was found for various anionic axial ligands. As reported previously,[20] a drastic axial ligand effect has been found for neutral axial ligands such as imidazole. The present mechanism for the anioic axial ligand effect would also be applicable to the neutral axial ligand effect. However, the correlation line for the neutral axial ligand would differ from the line for the anionic axial ligand shown here because the Fe-L bond character is different between the neutral ligand and the anionic ligand.

Structure and Electronic State of Transition State. As discussed above, the small α values for the reactions of $(TMP^{+\bullet})Fe^{IV}O(L)$ with cyclooctene, *N*,*N*-dimethyl-*p*-nitroaniline, and 1,4-cyclohexadiene indicate the existence of early transition states that are structurally close to the initial reactant state. Therefore, in the transition state, the oxo ligand still binds to the iron center and weakly interacts with the substrate. Previous studies proposed reaction mechanisms for epoxidation of cyclooctene and a demethylation reaction of dimethylaniline from the kinetic analysis, isotope experiments, and redox potentials of oxoiron(IV) porphyrin π-cation radical complexes.[21,33] In an epoxidation reaction, weak orbital interactions between cyclooctene and the Fe=O moiety of the oxoiron(IV) porphyrin π-cation radical complex may be formed at the transition state, and the electron transfer may occur in the bond formation process between the oxo-ligand of Fe=O and C=C moiety of olefin. On the other hand, the demethylation reaction by $(TMP^{+\bullet})Fe^{IV}O(L)$ was proposed to proceed via electron transfer followed by H-atom transfer which competes with back

dx.doi.org/10.1021/ic3006597 | *Inorg. Chem.* 2012, 51, 7296−7305

electron transfer. For *N*,*N*-dimethyl-*p*-nitroaniline, the H-atom of the methyl group of the formed amine radical would weakly interact with the Fe=O moiety. The small α value is consistent with the proposed transition states.

The α value for the hydrogen abstraction of $(TMP^{+\bullet})Fe^{IV}O(L)$ is smaller than the corresponding values for the epoxidation and demethylation reactions, and may suggest the existence of an early transition state. In the transition state, the Fe=O moiety of $(TMP^{+\bullet})Fe^{IV}O(L)$ would interact with the proton abstracted from 1,4-cyclohexadiene. However, the hydrogen atom tunneling effect must be considered for interpretation of the α value for the hydrogen abstraction reaction. A hydrogen abstraction reaction with a large $\Delta G^{\ddagger}$ value, such as for $(TMP^{+\bullet})Fe^{IV}O(NO_3)$, may proceed via not only a normal reaction pathway but also via a hydrogen atom tunneling pathway. This leads to a decrease in the α value.

The ground states of $(TMP^{+\bullet})Fe^{IV}O(L)$ and $(TMP)Fe^{III}(L)$ are quartet (S =3/2) and sextet (S = 5/2) states, respectively. Thus, the spin state must be switched from quartet to sextet in the reaction of $(TMP^{+\bullet})Fe^{IV}O(L)$. It is likely that this occurs near the transition state. Since the energy of the transition state is governed by the stability of the ground state of the product, as discussed above, the energy of the sextet state is a key to determining its reactivity. The sextet state has not been extensively studied as a transition state in previous theoretical studies.[35] In most cases, the ground (quartet) state and the lowest excited (doublet) states have been examined in efforts to explain the reactivity of compound I, and the doublet ground state was proposed for the transition state.[17,18] The present DFT calculations showed that the energies of the sextet states are 50−60 kJ/mol above the quartet (ground) states for $(TMP^{+\bullet})Fe^{IV}O(L)$, and these energies are close to the $\Delta G^{\ddagger}$ values determined at 213 K (Table 1 and 2). With the substrate coming close to and interacting with $(TMP^{+\bullet})Fe^{IV}O(L)$, the Fe=O bond of $(TMP^{+\bullet})Fe^{IV}O(L)$ becomes weaker and longer, and the energy of the quartet (ground) state increases. At last, the ground state is switched over from the quartet state to the sextet state near the transition state. After switching to the sextet state, the reaction would proceed along the energy surface of the sextet state and reach the sextet state of the final product of $(TMP)Fe^{III}(L)$.

The stabilization of the sextet state of $(TMP)Fe^{III}(L)$ by the axial ligand effect is also manifested in the energy of the sextet state of $(TMP^{+\bullet})Fe^{IV}O(L)$. The calculated energy gap between the quartet ground state and the sextet state which is changed by the axial ligand correlates with the $\Delta H^{\ddagger}$ value estimated for cyclooctene epoxidation for $(TMP^{+\bullet})Fe^{IV}O(L)$ in this study (Supporting Information, Table S4). The small energy gap between the sextet state of $(TMP^{+\bullet})Fe^{IV}O(L)$ and the $\Delta G^{\ddagger}$ value is reasonable with respect to the early transition state suggested from the present α values determined in this study.

Axial Ligand Effect in Heme Enzymes. The protein axial ligands of peroxidase, catalases and cytochrome P450 are histidine (imidazole), tyrosine (phenolate), and cystein (thiolate), respectively.[1,6,11] Since the five-coordinate ferric heme complexes of these heme enzymes are in the high spin (S = 5/2) state, as they are in the present model study, it is reasonable to expect that an axial ligand effect exists in these heme enzymes which is similar to that of the present model system. Since the fluoride axial ligand, the strongest ligand employed in this study, can be easily replaced by imidazole, phenolate, and thiolate ligands, the compound I intermediates of these heme enzymes would be more reactive than the present compound I model complexes. In fact, we recently showed that the reactivity of compound I model complexes with imidazole and phenolate axial ligands is 100−400-fold higher than that of the compound I model with nitrate as the axial ligand.[20] The very large negative shift of the redox potential for the Fe^{II}/Fe^{III} redox process for iron(III) porphyrin thiolate complexes (−1.19 V vs SCE) also indicates that the resting state is very stable.[36] This suggests that compound I of cytochrome P450 is much more reactive than compound I of peroxidases, catalases, and synthetic heme complexes. The mechanism by which compound I gains high reactivity by stabilizing the resting state, and not by destabilizing the compound I state, is expected to be convenient for the oxygenation reactions of heme enzymes because destabilization of compound I might lead to inactivation of the enzymes because of unfavorable side reactions involving oxidation of amino acid residues of the protein in the vicinity of the heme active site.

EXPERIMENTAL SECTION

Instrumentation. UV−visible absorption spectra were recorded on an Agilent 8453 spectrometer (Agilent Technologies) equipped with a USP-203 low-temperature chamber (UNISOKU). ^{1}H NMR spectra were measured on a Lambda-500 spectrometer (JEOL). Chemical shifts were referenced to the residual peak of dichloromethane, (5.32 ppm). The concentrations of NMR samples were 1−3 mM. EPR spectra were recorded in a quartz cell (d = 5 mm) on an E500 continuous wave X-band spectrometer (Bruker) with an ESR910 helium-flow cryostat (Oxford Instruments). Gas chromatography−mass spectroscopy (GC-MS) analysis was performed on a QP-5000 GC-MS system (Shimadzu) equipped with a capillary gas chromatograph (GC-17A, CBP5-M25-025 capillary column). Cyclic voltammograms and differential pulse voltammograms were measured with an ALS612A electrochemical analyzer in degassed dichloromethane containing 0.1 M nBu$_4$N$^+$ClO$_4^-$ (TBAP) as a supporting electrolyte. A glassy carbon electrode was used as the working electrode and a platinum-wire electrode was employed as the counter electrode. The potentials were recorded with respect to a saturated calomel electrode (SCE) as a reference electrode. Resonance Raman scattering was excited at 406.7 nm from a Kr^+ laser (Spectra Physics, BeamLok 2060), dispersed by a single polychromator (Ritsu Oyo Kogaku, MC-1000DG), and detected with a liquid-nitrogen cooled CCD detector (Roper Scientific, LNCCD-1100-PB). Laser power at the sample was 20 mW. The mechanical slit width was 200 μm. Sample concentrations (~1 mM) were prepared in an NMR tube (O.D. = 5 mm) at −80 °C and set in a custom-designed glass cell with optical windows, which was precooled at −80 °C with cold dry nitrogen gas. Resonance Raman spectra were measured with 135° backscattering geometry with rapid spinning of the sample tube.

Materials. Anhydrous dichloromethane was obtained commercially and stored in the presence of 4 Å molecular sieves. Cyclooctene and 1,4-cyclohexadiene were purchased commercially and used after passing through activated alumina immediately prior to use to remove polar impurities. Other chemicals were purchased commercially and used without further purification. *meso*-Tetramesitylporphyrin ($TMPH_2$) was prepared according to a previously published procedure.[39] $(TMP)Fe^{III}Cl$ was prepared by insertion of iron into $TMPH_2$ with $FeCl_2$ and sodium acetate in acetic acid, and purified with a silica gel column using CH_2Cl_2/CH_3OH as an eluent.[40] $(TMP)Fe^{III}Cl$ was passed through a basic alumina (10% water) column with dichloromethane as an eluent to produce $(TMP)Fe^{III}OH$.[21] The $(TMP)Fe^{III}(L)$ complexes were obtained from reactions of $(TMP)Fe^{III}(OH)$ with corresponding acids (F: hydrofluoric acid, Ac: acetic acid, Bz: benzoic acid, TFA: trifluoroacetic acid, Hc: hydrocinnamic acid, and NO_3: nitric acid) in toluene solution and purified by recrystallization from ether/n-hexane.[41]

dx.doi.org/10.1021/ic3006597 | Inorg. Chem. 2012, 51, 7296−7305

Kinetics and Product Analysis. $(TMP^{+\bullet})Fe^{IV}O(L)$ (100 μM) in dichloromethane was prepared in a 1 cm quartz cuvette in a low-temperature chamber in a UV−visible absorption spectrometer by bubbling O_3 gas at low temperature (−30 to −80 °C). After generation of $(TMP^{+\bullet})Fe^{IV}O(L)$, excess O_3 gas was removed by bubbling Ar gas. An excess (10−1000 equiv) of cyclooctene, 1,4-cyclohexadiene, or *N*,*N*-dimethyl-*p*-nitroaniline was then added to the solution with vigorous stirring, and the reactions were monitored by the absorption spectral change at constant time intervals. The reaction rate constants were determined by a curve fit of the time dependence of the absorbance of the peaks in the vicinity of 500 and 667 nm. The absorption spectral change followed the first-order kinetics in the presence of the large excess of substrates, and the second-order reaction rate constants (k_2) were determined from the linear dependence of the pseudo first-order rate constants on the concentrations of these substrates (Supporting Information, Figure S1). Activation of enthalpy ($\Delta H^{\ddagger}$) and activation of entropy ($\Delta S^{\ddagger}$) values for the cyclooctene epoxidation reactions by $(TMP^{+\bullet})Fe^{IV}O(L)$ were estimated from the Eyring plots (Supporting Information, Table S4). The free energy of activation ($\Delta G^{\ddagger}$) values were calculated from the second-order reaction rate constants with the relationship, $\Delta G^{\ddagger} = -RT\ ln(hk_2/kT)$.[42] The yield of cyclooctene oxide was determined by GC-MS using undecane as an internal standard. After completion of the reactions, 10 equiv of tetra-*n*-butylammonium iodide (n-$Bu_4N^+I^-$) was added to the reaction solutions at low temperature. The reaction mixture was taken from the low-temperature chamber and warmed to room temperature. After addition of undecane, the reaction mixture was analyzed by GC-MS. Yields of cyclooctene oxide were determined from a standard calibration curve prepared with authentic cyclooctene oxide.

Ligand Exchange. The relative energies for $(TMP^{+\bullet})Fe^{IV}O(L)$ and $(TMP)Fe^{III}(L)$ were estimated through the ligand-exchange reactions. Ligand-exchange reactions of $(TMP^{+\bullet})Fe^{IV}O(L_1)$ or $Fe^{III}(TMP)(L_1)$ with $nBu_4N(L_2)$ were monitored by using ^1H NMR spectra. Samples of $(TMP^{+\bullet})Fe^{IV}O(L_1)$ in CD_2Cl_2 for ligand-exchange reactions were prepared by ozone oxidation reactions in NMR tubes. To remove trace quantities of HCl, CD_2Cl_2 was passed through activated alumina just prior to use. $nBu_4N(L_2)$ compounds in CD_2Cl_2 were slowly titrated in the NMR tubes until the majority of the $(TMP^{+\bullet})Fe^{IV}O(L_1)$ complex was converted to $(TMP^{+\bullet})Fe^{IV}O(L_2)$. The addition of $nBu_4N(L^2)$ showed a spectral change, indicating the progression of the ligand-exchange reaction without reduction of the porphyrin π-cation radical.

The equilibrium constant, *K*, for the ligand-exchange reactions, $(TMP^{+\bullet})Fe^{IV}O(L_1) + nBu_4N(L_2) \rightleftarrows (TMP^{+\bullet})Fe^{IV}O(L_2) + nBu_4N(L_1)$, is defined as

$$K = ([(TMP^{+\bullet})Fe^{IV}O(L_2)][nBu_4N(L_1)]) / ([(TMP^{+\bullet})Fe^{IV}O(L_1)][nBu_4N(L_2)]) = \alpha^2/\{(1-\alpha)(n-\alpha)\}$$

where α denotes the molar fraction of $(TMP^{+\bullet})Fe^{IV}O(L_2)$ and *n* is the molar ratio of added $nBu_4N(L_2)$ over total heme. The α value for each titration experiment was determined from the peak areas for *m*-H, *o*-Me, *p*-Me, and pyrrole-H signals of $(TMP^{+\bullet})Fe^{IV}O(L_1)$ and $(TMP^{+\bullet})Fe^{IV}O(L_2)$. The *K* values were determined by performing a least-squares curve fit of the plot of α against *n*. The equilibrium constants (*K*) for $(TMP)Fe^{III}(L)$ for the ligand-exchange reactions, $(TMP)Fe^{III}(L_1) + nBu_4N(L_2) \rightleftarrows (TMP)Fe^{III}(L_2) + nBu_4N(L_1)$, were also estimated using the same method.

Quantum Chemical Calculations. The quantum chemical calculation was performed using the Gaussian09 program package.[43] The 6-31+G* basis set was used for the Fe atom. The 6-31G* basis set was used for the N atoms of the porphyrin and the atoms of the axial ligands, and the 6-31G basis set was used for the other atoms. The optimized structures and energies of the spin states were calculated using an unrestricted B3LYP density functional method.

■ ASSOCIATED CONTENT

Ⓢ Supporting Information

Figures S1−S10 and Table S1−S4. Complete ref 43. This material is available free of charge via the Internet at http://pubs.acs.org.

■ AUTHOR INFORMATION

Corresponding Author

*Phone: +81-564-59-5578. E-mail: hiro@ims.ac.jp.

Notes

The authors declare no competing financial interest.

■ ACKNOWLEDGMENTS

This study was supported by grants from JSPS (Grant-in-Aid for Scientific Research, Grant No. 22350030 to H.F. and No. 22018026 to T.O.) and MEXT (Global COE Program).

■ REFERENCES

(1) Sono, M.; Roach, M. P.; Coulter, E. D.; Dawson, J. H. *Chem. Rev.* **1996**, *96*, 2841−2887.

(2) Krebs, C.; Fujimori, D. G.; Walsh, C. T.; Bollinger, J. M., Jr. *Acc. Chem. Res.* **2007**, *40*, 484−492.

(3) Groves, J. T.; Han, Y.-Z. In *Cytochrome P450: Structure, Mechanism, and Biochemistry*; Ortiz de Montellano, P. R., Ed.; Plenum: New York, 1995; pp 3−48.

(4) Watanabe, Y.; Fujii, H. *Struct. Bonding (Berlin, Ger.)* **2000**, *97*, 61−89.

(5) Costas, M.; Mehn, M. P.; Jensen, M. P.; Que, L., Jr. *Chem. Rev.* **2004**, *104*, 939−986.

(6) Dunford, H. B. *Heme Peroxidases*; Wiley-VCH: New York, 1999.

(7) Schonbaum, G. R.; Chance, B. In *The Enzymes*; Boyer, P. D., Ed.; Academic Press: New York, 1979; Vol. *13*, pp 363−408.

(8) Gouet, P.; Jouve, H.-M.; Williams, P. A.; Andersson, I.; Andreoletti, P.; Nussaume, L.; Hajdu, J. *Nat. Struct. Biol.* **1996**, *3*, 951−956.

(9) Schlichting, I.; Berendzen, J.; Chu, K.; Stock, A. M.; Marves, S. A.; Benson, D. E.; Sweet, R. M.; Ringe, D.; Petsko, G. A.; Sligar, S. G. *Science* **2000**, *287*, 1615−1622.

(10) Rittle, J.; Green, M. T. *Science* **2010**, *330*, 933−937.

(11) Zamocky, M.; Furtmüller, P. G.; Obinger, C. *Antioxid. Redox Signaling* **2008**, *10*, 1527−48.

(12) Ohno, T.; Suzuki, N.; Dokoh, T.; Urano, Y.; Kikuchi, K.; Hirobe, M.; Higuchi, T.; Nagano, T. *J. Inorg. Biochem.* **2000**, *82*, 123−125.

(13) Gross, Z. *J. Biol. Inorg. Chem.* **1996**, *1*, 368−371.

(14) Higuchi, T.; Uzu, S.; Hirobe, M. *J. Am. Chem. Soc.* **1990**, *112*, 7051−7052.

(15) (a) Song, W. J.; Ryu, Y. O.; Song, R.; Nam, W. *J. Biol. Inorg. Chem.* **2005**, *10*, 294−304. (b) Kamachi, T.; Kouno, T.; Nam, W.; Yoshizawa, K. *J. Inorg. Biochem.* **2006**, *101*, 1464−1472. (c) Kang, Y.; Chen, H.; Jeong, Y. J.; Lai, W.; Bae, E. H.; Shaik, S.; Nam, W. *Chem.—Eur. J.* **2009**, *15*, 10039−10046. (d) de Visser, S. P.; Tahsini, L.; Nam, W. *Chem.—Eur. J.* **2009**, *15*, 5577−5587.

(16) Rydberg, P.; Sigfridsson, E.; Ryde, U. *J. Biol. Inorg. Chem.* **2004**, 203−223.

(17) (a) Kumar, D.; de Visser, S. P.; Sharma, P. K.; Derat, E.; Shaik, S. *J. Biol. Inorg. Chem.* **2005**, *10*, 181−189. (b) de Visser, S. P. *J. Biol. Inorg. Chem.* **2006**, *11*, 168−178. (c) Renyue, W.; de Visser, S. P. *J. Inorg. Biochem.* **2007**, *101*, 1464−1472.

(18) (a) de Visser, S. P. *J. Am. Chem. Soc.* **2010**, *132*, 1087−1097. (b) Kumar, D.; Karamzadeh, B.; Sastry, G. N.; de Visser, S. P. *J. Am. Chem. Soc.* **2010**, *132*, 7656−7667. (c) Kumar, D.; Sastry, G. N.; de Visser, S. P. *J. Phys. Chem. B* **2012**, *116*, 718−730.

(19) Prokop, K. A.; de Visser, S. P.; Goldberg, D. P. *Angew. Chem., Int. Ed.* **2010**, *49*, 5091−5095.

(20) Takahashi, A.; Kurahashi, T.; Fujii, H. *Inorg. Chem.* **2009**, *48*, 2614−2625.
(21) Takahashi, A.; Kurahashi, T.; Fujii, H. *Inorg. Chem.* **2011**, *50*, 6922−6928.
(22) Fujii, H. *Coord. Chem. Rev.* **2002**, *226*, 51−60.
(23) Scheidt, W. R.; Gouterman, M. In *Iron Porphyrins*; Lever, A. B. P., Gray, H. B., Eds.; Addison-Wesley: London, U.K., 1983; Part I, pp 89−139.
(24) Kadish, K. M.; Rhodes, R. K. *Inorg. Chem.* **1983**, *22*, 1090−1094.
(25) Jones, R. W.; Staley, R. H. *J. Am. Chem. Soc.* **1982**, *104*, 2296−2300.
(26) Operti, L.; Tews, E. C.; Freiser, B. S. *J. Am. Chem. Soc.* **1988**, *110*, 3847−3853.
(27) Brønsted, J. N. *Chem. Rev.* **1928**, *5*, 231−338.
(28) Eyring, H.; Polanyi, M. Z. *Z. Phys. Chem., Abt. B* **1931**, *12*, 279.
(29) Evans, M. G.; Polanyi, M. *Trans. Faraday Soc.* **1938**, *34*, 11−24.
(30) van Santen, R. A.; Neurock, M.; Shetty, S. G. *Chem. Rev.* **2010**, *110*, 2005−2048.
(31) Garrison, J. M.; Ostovic, D.; Bruice, T. C. *J. Am. Chem. Soc.* **1989**, *111*, 4960−4966.
(32) Shaik, S.; Lai, W.; Chen, H.; Wang, Y. *Acc. Chem. Rev.* **2010**, *42*, 1154−1165.
(33) Goto, Y.; Watanabe, Y.; Fukuzumi, S.; Jones, J. P.; Dinnocenzo, J. P. *J. Am. Chem. Soc.* **1998**, *120*, 10762−10763.
(34) (a) Groves, J. T.; McClusky, G. A. *J. Am. Chem. Soc.* **1976**, *98*, 859−861.
(35) (a) Schöneboom, J. C.; Neese, F.; Thiel, W. *J. Am. Chem. Soc.* **2005**, *127*, 5840−5853. (b) Hirao, H.; Kumar, D.; Thiel, W.; Shaik, S. *J. Am. Chem. Soc.* **2005**, *127*, 13007−13018.
(36) Tani, F.; Matsu-ura, M.; Nakayama, S.; Ichimura, M.; Nakamura, N.; Naruta, Y. *J. Am. Chem. Soc.* **2001**, *123*, 1133−1142.
(37) Czarnecki, K.; Nimri, S.; Gross, Z.; Proniewicz, L. M.; Kincaid, J. R. *J. Am. Chem. Soc.* **1996**, *118*, 2929−2935.
(38) Paeng, K.-J.; Shin, D.-H.; Paeng, I. R. *Inorg. Chem.* **1997**, *36*, 2901−2903.
(39) Lindsey, J.; Wagner, R. *J. Org. Chem.* **1989**, *54*, 828−836.
(40) Fujii, H. *J. Am. Chem. Soc.* **1993**, *115*, 4641−4648.
(41) Fuhrhop, J.-H.; Smith, K. M. In *Porphyrins and Metalloporphyrins*; Smith, K. M., Ed.; Elsevier: Amsterdam, The Netherlands, 1975; pp 757−869.
(42) Eyring, H. *J. Chem. Phys.* **1935**, *3*, 107−115.
(43) Frisch, M. J. et al. *Gaussian09*, Revision A.1; Gaussian, Inc.: Wallingford, CT, 2009.